

Exploiting the Sentinel-3 tandem phase dataset and azimuth oversampling to better characterize the sensitivity of SAR altimeter sea surface height to long ocean waves

P. Rieu^a, T. Moreau^a, E. Cadier^a, M. Raynal^a, S. Clerc^b, C. Donlon^c, F. Borde^c,
F. Boy^d, C. Maraldi^d

^a CLS, 11 rue Hermès, Parc Technologique du Canal, 31520 Ramonville St Agne, France

^b ACRI-ST, 260 Route du Pin Montard, 06410 Biot, France

^c ESA/ESTEC, Keplerlaan, 1, 2201 AZ Noordwijk, The Netherlands

^d CNES, 18 avenue Edouard Belin, 31401 Toulouse Cedex 9, France

Received 15 June 2020; received in revised form 19 September 2020; accepted 24 September 2020
Available online 9 October 2020

Abstract

Being the very first SAR mode altimeter tandem phase, the Sentinel-3 A/B tandem phase has provided an unprecedented opportunity to better characterize the sensitivity of SAR altimetry retrievals to high-frequency processes, such as long ocean waves. In this paper, we show that for some sea-state conditions, that are still to be precisely characterized, long ocean waves are responsible for high-frequency (spatial and temporal) coherent Sea Level Anomaly (SLA) signals. It is found that the peak wavelength corresponds to the dominant swell wavelength. Furthermore, the short time lag between S3-A and S3-B acquisitions allows performing cross-spectral analyses that reveal phase shifts consistent with waves travelling according to the wave dispersion relation. It is also demonstrated that the classical 20 Hz sampling frequency is insufficient to properly sample most swell-induced SLA signals and that aliasing can generate errors over the entire frequency spectrum, including at long wavelengths. These results advocate for the use of azimuth oversampling (40 Hz or 80 Hz). Low-pass filtering should be applied prior to any down-sampling to 20 Hz, in order to prevent long-wavelength errors induced by spectral leakage.

© 2020 COSPAR. Published by Elsevier Ltd. All rights reserved.

Keywords: SAR altimetry; Sea surface height spectrum; Swell; Sentinel-3 tandem phase

1. Introduction

Sentinel-3 is a twin-satellite mission providing global coverage and high-quality data delivery for the Copernicus environmental monitoring programme (Donlon et al., 2012). Sentinel-3B, the second satellite of this system, has been successfully launched in April 2018. Before being

inserted into its final orbit (at $\pm 140^\circ$ to its twin, Sentinel-3A), it has been positioned in a four-month-long close formation with Sentinel-3A, during which the two satellites were observing the same scene approximately 30 s apart. This flight configuration allowed to perform a very accurate cross-calibration of the Sentinel-3 constellation instruments, in order to produce homogeneous and unbiased time-series observations for climate record (Clerc et al., 2020), as it was done before for the Jason series (Dibarbouré et al., 2011). The two identical instrument payloads include a Synthetic Aperture Radar (SAR) altimeter (also known as Delay-Doppler altimeter) that continuously measures the sea-surface topography with

E-mail addresses: prieu@groupcls.com (P. Rieu), tmoreau@groupcls.com (T. Moreau), ecadier@groupcls.com (E. Cadier), mraynal@groupcls.com (M. Raynal), sebastien.clerc@acri-st.fr (S. Clerc), craig.donlon@esa.int (C. Donlon), franck.borde@esa.int (F. Borde), francois.boy@cnes.fr (F. Boy), claire.maraldi@cnes.fr (C. Maraldi)

unprecedented accuracy, precision and resolution (Raney, 1998; Wingham et al., 2006; Boy et al., 2017a). SAR altimeters provide valuable observations of the sea surface features at small scales, which were not accessible with conventional pulse-limited radar altimeters (Dibarboure et al., 2014).

These improvements are achieved by exploiting the Doppler information within a burst of pulses. The unfocused SAR processing allows to synthesize Doppler beams with increased along-track-resolution (Raney, 1998; Scagliola, 2013), that are subsequently combined (multi-looked) to reduce the speckle noise affecting the waveforms. As a result, SAR altimetry provides both better resolution and lower measurement noise on the estimated parameters (SSH, SWH, sigma naught) (Raynal et al., 2018a).

Identifying and evaluating the different sources of uncertainty affecting the SAR altimeter measurements is essential, as SAR altimetry will be increasingly used in the future (as it is the case for the upcoming Sentinel-3C/D and the Sentinel-6 missions), thus contributing strongly to the time series of ocean topography measurements. Sea state effects predominantly contribute to the uncertainty in the ocean height retrievals (Chelton et al., 2001; Ardhuin et al., 2019). The measurement noise on the estimates, induced by the radar speckle noise and usually characterized by the 1 Hz dispersion, increases with the significant wave height (SWH) (Halimi et al., 2014; Ray et al., 2015), like in conventional altimetry. The accuracy of the measurement is also impacted through the sea-state bias (SSB), that leads to wave height dependent errors in the SSH estimation. Corrections to mitigate this effect are applied (Tran et al., 2010; Pires et al., 2016) and can be complemented by high-frequency adjustment (HFA) corrections to remove the residual short-scale correlated error between the range and SWH estimates (Zaron and deCarvalho, 2016; Tran et al., 2020). Today, sea state bias remains the largest source of uncertainty for satellite altimetry over the ocean.

Additionally, SAR altimeter retrievals have been reported to be sensitive to the presence of long swells by different authors (Aouf and Phalippou, 2015; Abdalla and Dinardo, 2016; Moreau et al., 2018, Reale et al., 2018). Concerning SWH, systematic biases with respect to wave models and conventional altimetry have been observed. The impact depends strongly on the period of the waves and their energy, but also on the orientation of the satellite track with respect to them (with increased effects for waves traveling up or down the track). Unlike SWH, no such systematic biases were reported for the SSH. Another important effect of swell is the increase of the high-frequency noise (dispersion around the 1 s average) on the estimated parameters (SSH, SWH and, to a lesser extent, sigma naught). It has been attributed to direct sensitivity to the wave surface topography, whose scale is comparable to the size of the altimeter footprint in the SAR case (Moreau et al., 2018). Reale et al. (2018)

suggested that most SSH signals induced by the wave undulations could be aliased in the 20 Hz SAR data. Depending on the wave period and because of aliasing, such signals might not contribute only to the 1 Hz dispersion, but also to the variance at longer wavelengths. These results somehow concur with the analyses of the SAR altimeter SSH spectrum (Raynal et al., 2018b; Vergara et al., 2019), which have reported a red-colored noise from medium (around 100 km) to small wavelengths, whose characteristics depend on the sea-state properties and exhibit seasonal and regional variations that are correlated to the swell ones (Chen et al., 2002). The possible impact of swell on the long-wavelength SSH variance is of great importance and still needs to be clarified. It constitutes the main motivation of the present study.

In an attempt to going further into the characterization of the sensitivity of SAR altimeter data to long ocean waves, the present analysis exploits the Sentinel-3 tandem phase dataset, which has provided for the first time two SSH signals acquired by two identical SAR altimeters on very close ground tracks and with a time lag of about 30 s. This observation time lag is well suited for studying wind-generated surface gravity waves because their period ranges from 1 to 30 s (Holthuijsen, 2010), meaning that the waves have propagated by at least one wavelength between the two acquisitions. The main novelty of this study is to use the time lag to identify signals related to rapidly evolving phenomena on the sea surface, like propagating swells, in order to complement results obtained with mono-satellite observations. The methodologies used in this analysis are applied to Sentinel-3A and Sentinel-3B SRAL sea surface height data processed at the nominal rate, 20-Hz, and at a higher rate, 80-Hz (i.e. a spacing between two consecutive along-track measurements of about 340 m and 85 m respectively), in order to investigate possible aliasing effects impacting the measured signals.

The outline of this paper is as follows: Section 2 describes the datasets and the methodologies used for the analysis. Results are presented in Section 3, analyzing first some individual cases that are representative of the dataset and then extending the analysis to the global dataset. Section 4 discusses the results as well as possible processing strategies to remove SSH errors induced by long ocean waves. Finally, the main conclusions are drawn in the last section.

2. Data and methods

The altimetry data used in this study has been processed with the CNES Sentinel-3 Processing Prototype (S3PP), inherited from the Cryosat-2 Processing Prototype (Boy et al., 2017a). The processor has been validated over global ocean and achieves performances comparable to the Sentinel-3 operational ground segment (PDGS) (Raynal et al., 2018a). The starting point of the processing is the L1a dataset, provided by the Sentinel-3 ground segment, which contains the full-resolution 80 Hz acquisition made

by the SRAL altimeter. Reprocessing the data from L1a to L2 was necessary because the nominal 20 Hz sampling frequency was found to be insufficient to properly sample some high-frequency sea level signals correlated to the presence of swell, as explained further in the paper. Increasing the sampling frequency from 20 Hz to 40 Hz (or even 80 Hz) has already been investigated on before (Dinardo et al., 2014; Buchhaupt, 2019, ch. 5), showing that it brings some improvement on the precision of the estimated parameters in open ocean, and other areas (Egido et al., 2020; Aldarias et al., 2020). Sentinel-3 operational products are processed at 20 Hz, but it is possible for users to process on-demand Sentinel-3 data at higher sampling using the ESA G-POD Service, with two distinct SAR altimetry processors available (Dinardo et al., 2016; Buchhaupt et al., 2018). It is worth noting that the only effect of increasing the azimuth sampling frequency is to increase the number of samples in the dataset, while the SAR processing applied to the data is left completely unchanged.

The Sentinel-3 A/B tandem phase spans an overall period of more than four months, during which Sentinel-3A remained in its nominal operating mode: SAR mode with Open-Loop (OL) tracking (Le Gac et al., 2019) over open ocean (Clerc et al., 2020). Sentinel-3B has changed its mode several times for inter-calibration purposes, leaving approximately 54 days in which both altimeters acquired data in SAR/OL mode. To prevent any discrepancies coming from the use of different operating mode, we chose to focus on ten consecutive days (from 12/09/2018 to 22/09/2018) from this period. Over the studied period, Sentinel-3B flew ahead of Sentinel-3A by approximately 31 s (values range from 30.7 s to 31.1 s). The across-track separation of each satellite ground track was maintained by flight operations to ± 1 km during the tandem phase (Donlon et al., 2012). We have found that in practice the across-track separation between the ground tracks ranges from 200 to 450 m in the dataset that has been used for the present study.

In the analysis, we consider only uncorrected SLA, which is the difference between the altitude and the range value from the retracker, from which the value of the Mean Sea Surface (MSS) from CNES/CLS15 grids is subtracted. Not considering geophysical corrections on the range should not introduce any discrepancies given the very small temporal and spatial separation between S3A and S3B measurements, compared to the typical time and spatial scales of these corrections. Contrary to previous tandem phase analyses (Dibarboue et al., 2011), the collocation process has been kept to the strict minimum: Sentinel-3A 80 Hz samples are interpolated on the Sentinel-3B 80 Hz samples with a simple nearest-neighbor (in space) interpolation. Nearest-neighbor interpolation was chosen to avoid data resampling and the undesirable low-pass filtering that it implies.

The altimetry dataset has been collocated in space and time with the WaveWatch-III (WW3) wave model to get

external information on the sea-state. The WW3 model is run with ECMWF operational analyses forcing and is provided on $0.5^\circ \times 0.5^\circ$ global grids at 3 h time steps. The products are publicly available on the Ifremer FTP server (ftp://ftp.ifremer.fr/ifremer/ww3/HINDCAST/GLOBAL/2018_ECMWF/). More information on the wave model can be found in Rascle and Ardhuin (2013). The wave model significant wave height (SWH) has been collocated with 1 Hz altimeter measurements using linear interpolation (in space and time). To support the spectral analyses, we have extracted the available information about the wave spectrum: the one-dimensional wave spectrum and the first three partitions of the two-dimensional spectrum. The partitioning technique provides a decomposition of the two-dimensional spectrum into independent wave systems, which are either flagged as wind-sea partitions or swell partitions (Portilla et al., 2009). Wind-sea waves are locally generated waves, with generally broad frequency and angular distribution and contribute to the higher frequencies of the spectrum. Conversely, swells are remotely generated waves, with relatively narrow spectrum and lower frequencies than wind-sea waves (Holthuijsen, 2010). For each partition, we have extracted the peak period T_p , the partition significant wave height H_s and the direction θ . As spectral parameters representing a whole 1000 km long segment were needed for the comparison with altimeter data (spectral estimates from altimeter data need averaging over the whole segment), we chose to extract the model wave spectrum parameters (1D spectrum, partitions) at the center of the segments, because averaging is not suitable for these parameters.

The method used to select the dataset on which the SLA spectral analyses are performed is described in Dibarboue et al. (2014). A set of 1000 km long SLA segments (corresponding to 12,288 samples at 80 Hz), free of outliers, has been selected. Fig. 1 shows the geographical repartition of the 985 segments that constitute the dataset. The mean global Power Spectrum Density (PSD) is obtained by averaging the periodograms of the segments. Linear detrending and windowing with a Tukey window (alpha parameter set to 0.1) is applied when computing the periodograms in order to reduce boundary effects (Vergara et al., 2019).

The spectral analysis of each individual segment, aiming at detecting some high-frequency signal to be compared with the WW3 wave spectrum, is performed with a Welch method (Welch, 1967). This method allows reducing the noise on the estimated spectrum in exchange for reducing the frequency resolution. Each segment of 12,288 samples is split into 23 overlapping sub-segments of length 1024 (corresponding to approximately 87 km). The spectrum estimate is then obtained as the average of the periodograms of all the sub-segments. As recommended in Welch (1967) and Carter et al. (1973), a Hann window is applied in conjunction with a 50% overlapping parameter for optimal estimation. This method is used to

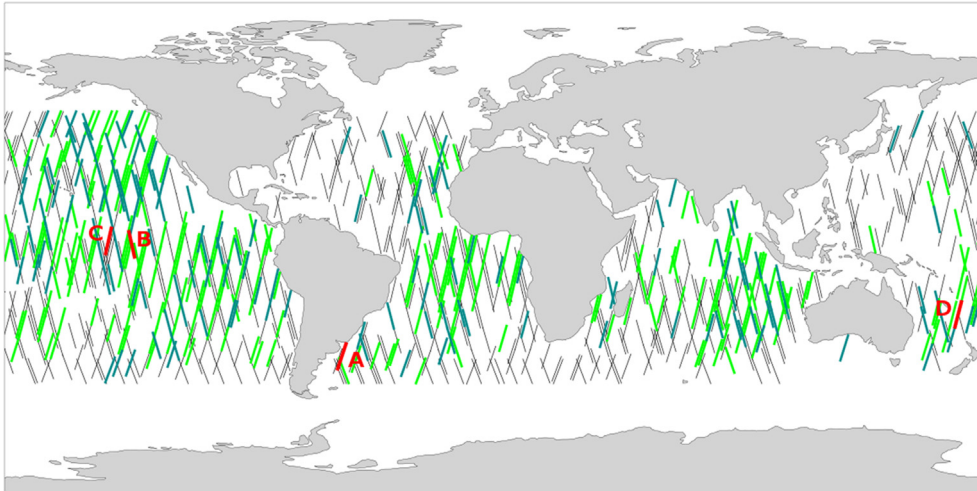


Fig. 1. Map showing the segments used for the spectral analysis. The color of the segments refers to the classification of the segments introduced further in the text (no high frequency coherence in black, significant high-frequency coherence and increasing phase shift in dark cyan, significant high-frequency coherence and decreasing phase shift in light green). The four segments used for the case studies are in red. (For interpretation of the references to color in this figure legend, the reader is referred to the web version of this article.)

compute estimates of the Power Spectrum Density (PSD), the Cross-Spectrum Density (CSD) and the Magnitude-Squared Coherence (MSC), which is the modulus of the CSD normalized by the PSDs. In the following, we will discuss mainly the coherence (MSC), a real-valued function between 0 and 1 that measures the correlation of the spectral components of the two time series, and the phase shift (the argument of the cross-spectrum density), that characterizes the delay between these spectral components.

The dataset has a relatively homogeneous geographical distribution (as shown in Fig. 1) but it represents a small period (only ten days). The climatology of swell having strong seasonal variations (Chen et al., 2002), statistics on the occurrence of swell might not be representative. Nevertheless, the global distribution over the open ocean ensures a wide variety of the sea states conditions. Fig. 2 shows the histogram of the significant wave height, showing good agreement between altimetry data and the WW3 model.

3. Results

The results of the spectral analysis are presented in three different parts. First, we explain the parameters that are considered and how the wave spectrum helps in interpreting the results, using the wave dispersion relation. Then, we present four segments that have been selected to be representative of the different cases encountered in the dataset, highlighting the correlation between the presence of some high-frequency coherent SLA signal and the presence of swell. Finally, we present the results for the whole dataset and we analyze the spectral signature of such events on the mean global SLA spectrum.

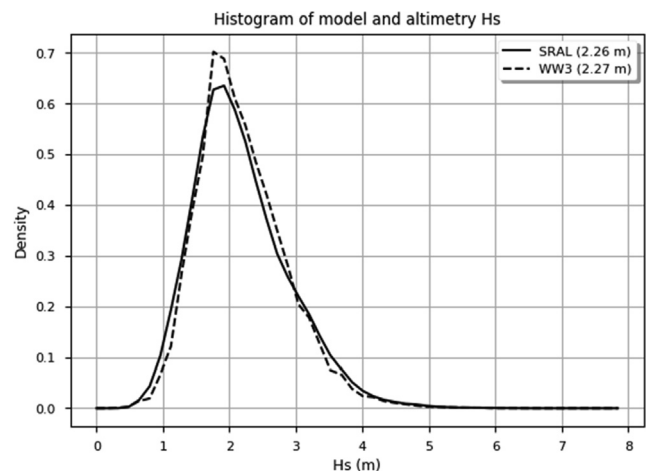


Fig. 2. Histogram of the significant wave height from S3 SRAL altimeter and WW3 wave model.

3.1. Interpretation of the SLA spectra with the wave spectrum

The SLA spectral estimates (PSDs, coherence and phase shift) obtained after applying the Welch method to the 1000 km long segments are interpreted using the wave model. We rely on the one-dimensional wave spectrum (taken at the center of the segment), given as a function of the wave frequency. We also use the information about the wind-sea partition and the first two swell partitions (if any). The extracted parameters are the peak period of the partition T_p , the significant wave height of the partition H_s and the propagation angle θ . The propagation angle is computed with respect to the satellite track, with the convention that 0° corresponds to waves propagating in the same direction as the satellite (down-track).

Without any influence of the swell, we expect to observe decreasing PSDs (with wavenumber), just as it is the case for the mean global spectrum (Dibarboure, 2014). For the long-wavelength geophysical signal, we expect high coherence values and zero phase shift. Indeed, both altimeters should measure the same long-wavelength geophysical signals as the twin SRAL altimeters (designed and operated identically) fly almost the same track with a time separation much smaller than the evolution time scale of these signals. For the small scales, the signal is expected to be dominated by measurement noise originating from the radar speckle noise on the waveforms. The speckle decorrelation time due to the sea surface motion, typically a few milliseconds (Boisot et al., 2016), is much smaller than the time lag between the acquisitions, guaranteeing that the measurement noise on the estimated parameters is completely uncorrelated. Thus, the coherence is expected very low (but not zero because the coherence estimator has a positive bias, as discussed further in the paper) and the phase shift uniformly distributed.

In the presence of some pure unidirectional swell oriented along the track, we expect the surface undulations to induce a peak on the SLA power spectra close to the peak wavenumber of the swell. Additionally, as the time lag between S3A and S3B acquisitions has the same order of magnitude as the period of the waves, we expect to observe time-coherent signals and thus an increase of the measured S3A/S3B coherence near the swell peak wavenumber. Then, we expect to observe a non-zero phase shift between the two signals as the waves propagate between the measurements. The measured phase shift should be governed by the phase velocity of the waves.

To perform comparisons between the SLA spectra and the wave model, we use the dispersion relation for unidirectional linear deep-water waves, which relates the angular frequency ω and the wavenumber k :

$$\omega = \sqrt{gk} \tag{1}$$

The deep-water assumption is valid for the ocean cases examined here, since the water depth is larger than half of the wavelength of the waves. According to this relation, the peak wavenumber of the swell k_p and the phase shift $\Delta\varphi$ are given by:

$$k_p = \frac{4\pi^2}{gT_p^2} \tag{2}$$

$$\Delta\varphi = \Delta t \sqrt{gk} \tag{3}$$

In the above expressions, T_p is the swell peak period and Δt is the time lag. Note that the sign of the phase shift depends on the propagation direction of the waves.

The peak wavenumber of the partitions is readily comparable to possible peaks in the SLA power spectrum, and the predicted phase shift (function of the wavenumber) should be close to the measured phase shift, for wavenumbers close to the swell peak wavenumber.

3.2. Case analysis

We focus on four different segments, denoted A, B, C and D. These segments appear in red in the map of Fig. 1 and information about the localization is given in Table 1. The results are gathered in Fig. 3, with the SLA spectral estimates plotted on the left-hand side and the model wave spectrum on the right-hand side.

3.2.1. Case A

The wave spectrum is dominated by a swell partition with a moderate period (11.4 s, corresponding to a wavelength of about 200 m), a relatively broad frequency spread and a propagation angle of 51° with respect to the ground track. There is no noticeable impact on the SLA estimates: no peak on the PSDs, low coherence and random phase shift. The high-frequency SLA signal seems completely dominated by incoherent noise. We further notice a significant drop of the PSDs for wavenumbers greater than 1/0.3 cpkm. This behavior, already observed in (Buchhaupt, 2019, ch. 5), is the consequence of the azimuth oversampling (1/0.3 cpkm is the cutoff wavenumber corresponding to the azimuth resolution of the processing).

3.2.2. Case B

The swell (partition 1) has a much longer period (17.5 s, equivalent to 490 m in wavelength), a smaller frequency spread and propagates approximately down-track (20° angle). The wind-sea partition is relatively more important compared to case A. We observe this time a broad bump on the SLA spectrum, approximately centered on the peak wavenumber of the swell partition. Concerning the cross-spectral parameters, we notice a significant increase of the coherence around the peak wavenumber, and the measured phase shift is in good agreement with the prediction of the dispersion relation. It is worth noting that the swell partition has a low significant wave height compared to case A.

3.2.3. Case C

The spectrum is dominated by the wind-sea partition, but there is a sharp swell partition (partition 2) with long period (16.5 s) and perfectly oriented up-track. In spite of the very small significant wave height of the swell partition (0.5 m), we have for this case also a bump on the power spectrum and an increase of the coherence. We notice that the bump is sharper than in case B and that the phase shift

Table 1
Localization of the segments for cases A, B, C and D.

Case	S3A Cycle/Track	Ascending/Descending	Localization
A	36 / 76	Descending	SW Atlantic
B	35 / 639	Ascending	Pacific
C	35 / 654	Descending	Pacific
D	36 / 144	Descending	SW Pacific

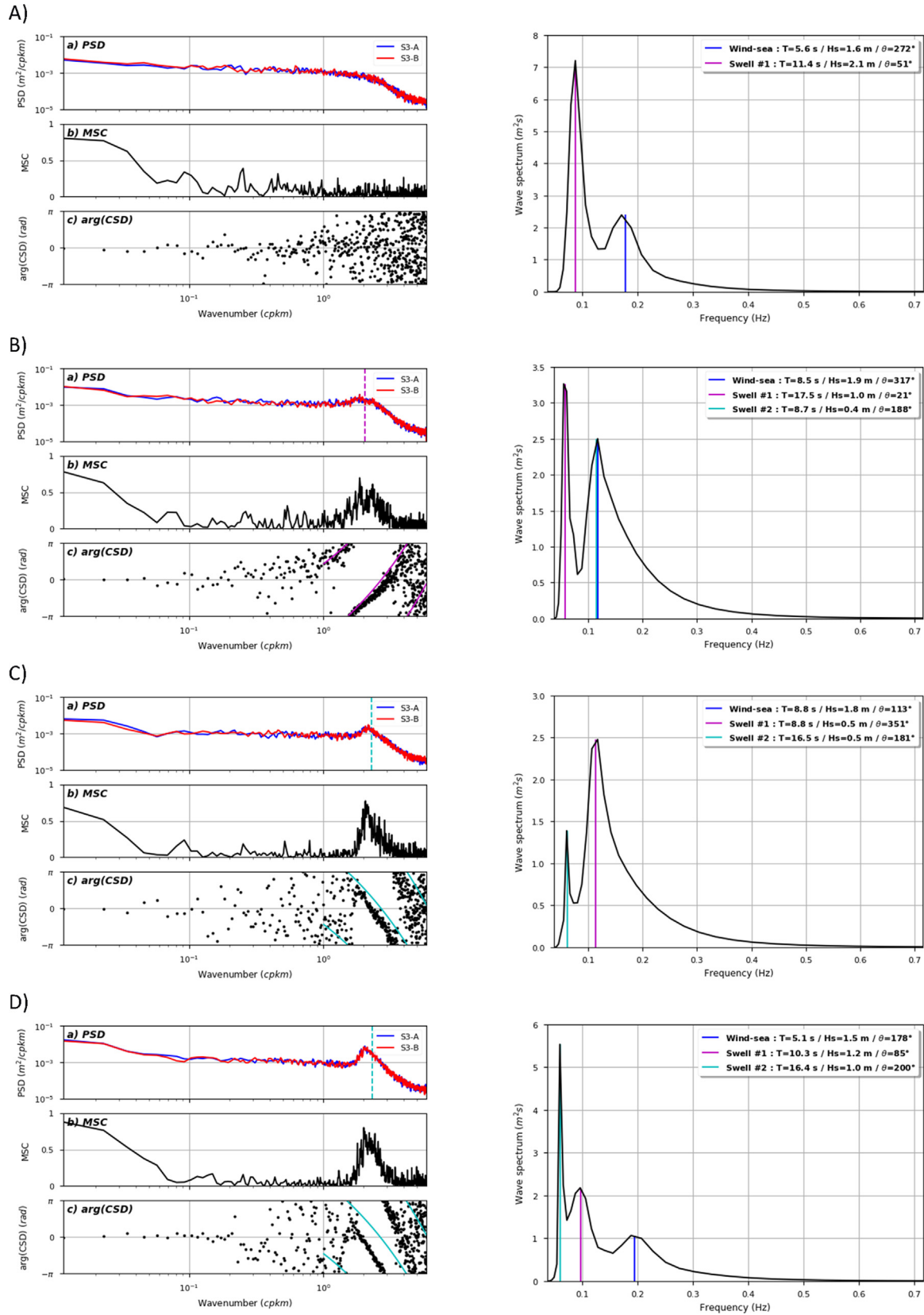


Fig. 3. (left) Plots of the spectral analysis parameters (a) PSD (b) coherence (c) phase shift for cases A, B, C and D. (right) WW3 one-dimensional wave spectrum as a function of wave frequency. The partitions of the spectrum are listed in the legend, with the peak period T_p , the significant wave height H_s and the propagation angle θ .

has an opposite sign, as expected because the swell propagates down-track in case B and up-track in this case. There seems to be a small constant phase shift bias compared to the prediction of the dispersion relation.

3.2.4. Case D

The spectrum has a strong swell partition (partition 2) with long period (16.4 s) and approximately oriented up-track. The resulting SLA bump is higher than case C, but it is no more centered on the peak wavenumber of the swell partition (it is shifted towards smaller wavenumbers). Concerning the phase shift, we notice this time a significant departure with respect to the prediction.

These results indicate that favorably oriented swells (up-track or down-track) with sufficiently long periods can generate high-frequency components in SLA spectrum for wavenumbers close to the swell peak wavenumber. As illustrated with the different cases, the significant wave height of the swell partition and the relative importance with respect to the wind-sea or other swell systems are not necessarily high. The measured signals are delayed because of the time lag between the two acquisitions, and the delay is in good agreement with the phase velocity of the waves predicted by the linear deep-water wave dispersion relation. Some small errors might be due to a geometrical effect coming from the misalignment of the swell propagation direction and the ground track. This effect could be investigated in future studies. More importantly, as discussed further in the paper, we believe that the SAR altimeter measurement over long swells is probably more complicated than a direct measurement of the wave topography along the ground track. Firstly, the height estimation relies on the whole waveform, which corresponds to a footprint which cross-track extension is more than 15 km. In addition to this, potential effects impacting the SAR measurement process, listed further in the discussion, could be responsible for the observed discrepancies.

3.3. Global analysis

The methodology presented in the previous section has been applied to the whole dataset in order to determine, for each segment, whether it is like case A (only incoherent measurement noise) or like case B, C and D (significant high-frequency coherence). To do so, we have computed for each segment the average value of the MSC for wavenumbers greater than 1 cpkm. As the MSC is estimated on sub-segments of 1024 samples with sampling frequency equal to $1/0.17\text{km}^{-1}$, the averaging is performed over the 425 highest wavenumber MSC samples. The histogram of the result is shown in Fig. 4.

Then, Monte-Carlo simulations have been performed to obtain the expected distribution of the coherence for white uncorrelated Gaussian noise. Following the method presented in Carter et al. (1973) and adapting it to the Welch method applied on the real data (size of segments,

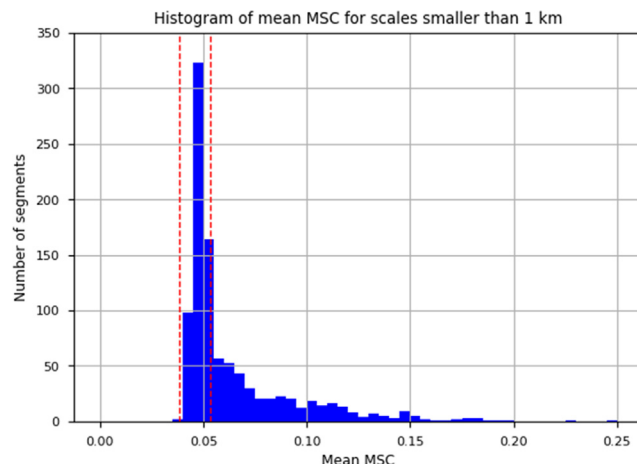


Fig. 4. Histogram of the average MSC value (computed for scales smaller than 1 km). Dashed red vertical lines correspond to the confidence interval obtained for uncorrelated white Gaussian noise. (For interpretation of the references to color in this figure legend, the reader is referred to the web version of this article.)

overlapping and window parameters), we obtained that the expected coherence is normally distributed with mean value $\mu = 0.046$ and standard deviation $\sigma = 0.0026$. As noted in Carter et al. (1973), the coherence estimator is biased: the expected value of the measured coherence is not zero. To detect the segments where the measured coherence is too high to be imputable to the measurement noise (and thus related to swell-induced signal), we use the classical $\mu \pm 3\sigma$ confidence interval of the expected coherence. The bounds of this interval are materialized with the dashed red vertical lines in Fig. 4.

As expected, the distribution of the MSC measured on the SLA segments has a thick right-hand tail; in other words, there is a significant proportion of the segments (38% of the whole dataset) that fall out of the confidence interval. This proves that, even if segments like case A (measured coherence in line with the expectation for uncorrelated noise) are a majority, significantly high coherence values (as observed for example in cases B, C and D), that have been associated with an impact of swell waves, are not isolated cases.

The color of the segments on the map of Fig. 1 depends on the value of the high-frequency coherence. The segments where the average MSC is inside the confidence interval are plotted in black. The other ones are plotted in dark cyan or light green, depending on whether the phase shift increases with the wavenumber or decreases. The analysis should be extended to a longer period to draw firm conclusions about the geographical distribution of the segments exhibiting high-frequency coherence. Yet, it is interesting to note that most of the green and cyan segments are in the eastern ocean basins (especially in the Pacific and the Indian oceans), where most of developed swells are encountered. Furthermore, we notice that increasing phase shift segments (dark cyan) are predominantly extracted from ascending passes, whereas the

decreasing phase shift segments (light green) correspond mostly to descending passes. These observations are consistent with the swell climatology (Chen et al., 2002). Indeed, at this time of the year (September), swells are mostly generated in the Southern Ocean and propagate northward with bended trajectories towards the East.

Using the partitioning criterion based on the average high-frequency coherence, we have computed the mean SLA spectrum for each of the two classes of segment. The spectra are computed both at 80 Hz (using all the available samples) and at 20 Hz (direct decimation). The S3-A SLA spectrum is shown on the left-hand side of Fig. 5 (the S3-B spectrum is not shown, but similar) and the spectrum of the SLA difference (S3-A minus S3-B) is plotted on the right-hand side. The mean spectra computed over the segments with significant high-frequency coherence are plotted in cyan, and the other ones are plotted in black. Both the 20 Hz and the 80 Hz spectra are plotted in Fig. 5; 20 Hz spectra extend up to $1/0.68\text{cpkm}$ whereas 80 Hz spectra extend up to $1/0.17\text{cpkm}$.

The distribution of the SWH in each of the two classes of segments is shown in Fig. 6. For both classes of segments, we observe very good agreement between altimeter measurements and the wave model. We note that the mean SWH is almost the same in the two classes of segment (approximately 10 cm higher for the no-coherence class).

The first observation that can be done on the SLA spectra (left-hand side of Fig. 5) is that the mean geostrophic signal spectrum is not identical for each of the two datasets, as the black and cyan curves do not coincide for wavenumbers smaller than 0.01cpkm . This is not abnormal as the segments from the two datasets are not identically distributed in space and span a relatively short period.

However, we observe that the SLA spectra (at 80 Hz) coincide for wavenumbers higher than 0.1cpkm , except for a bump located near 3cpkm . This bump is the manifestation, on the global spectrum, of the bumps that were already observed on cases B, C and D. It is interesting to

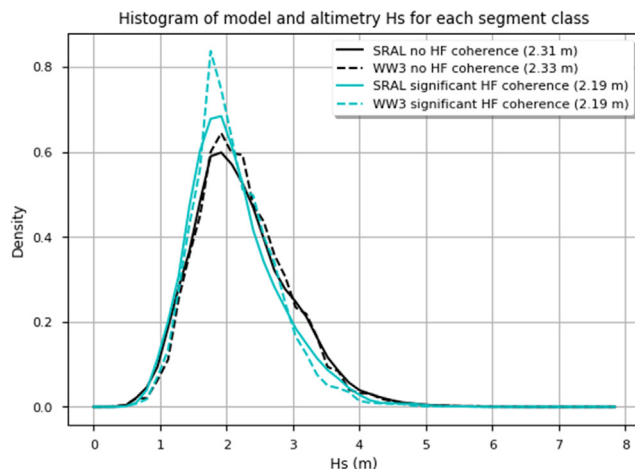


Fig. 6. Histogram of the significant wave height from S3 SRAL altimeter and the WW3 wave model. Cyan and black curves represent respectively segments with and without significant high-frequency coherence. (For interpretation of the references to color in this figure legend, the reader is referred to the web version of this article.)

note that the bump is entirely located over wavenumbers that are not properly sampled with the classical 20 Hz sampling frequency (i.e. wavenumber higher than $1/0.68\text{cpkm}$). The consequence is that this signal is aliased to smaller wavenumbers at 20 Hz, and it explains why the cyan 20 Hz spectrum is slightly higher than the black one for wavenumbers higher than 0.1cpkm (unlike the 80 Hz spectra).

Looking at the spectra of the SLA difference is even more instructive (right-hand side of Fig. 5), as the long-wavelength in-phase coherent geophysical signal should vanish in the subtraction whereas the variances of the measurement noise should add. The SLA difference spectrum therefore contains either incoherent noise or out of phase coherent signal. For the 80 Hz case, spectra are perfectly flat with the same variance up to 1cpkm . The bump originating from the coherent (out of phase) geophysical signal

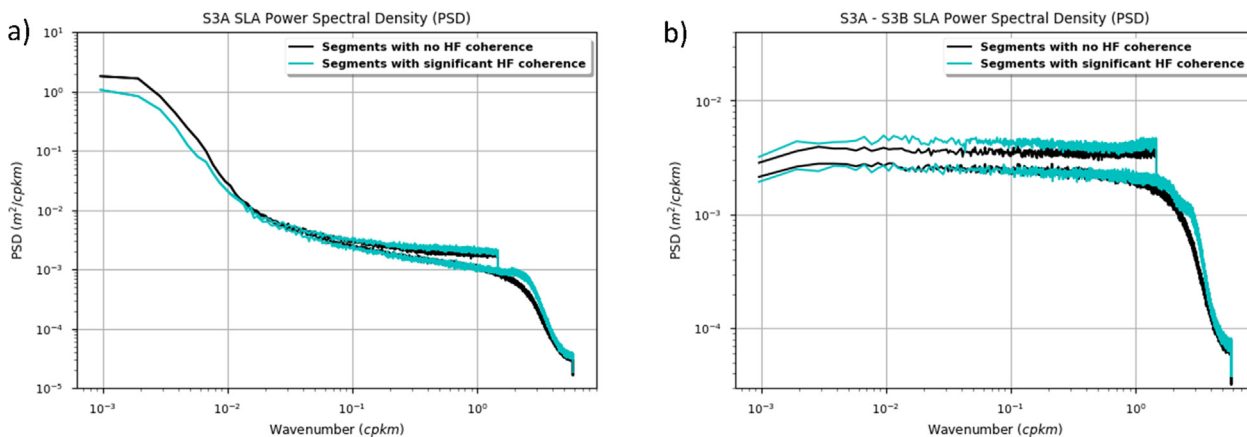


Fig. 5. Mean S3-A SLA spectrum (a) and SLA difference (S3-A – S3-B) spectrum (b) at 20 Hz and 80 Hz sampling frequencies. The cyan and black curves correspond respectively to the dataset with and without significant high-frequency coherence. (For interpretation of the references to color in this figure legend, the reader is referred to the web version of this article.)

is visible on the cyan curve for wavenumbers higher than 1 cpkm. The fact that the 80 Hz black and cyan spectra coincide up to 1 cpkm is expected, since the mean SWH is almost the same for the two classes of segment and the variance of the measurement noise theoretically depends only on the SWH, as explained in Halimi et al. (2014). On the contrary, the 20 Hz cyan difference spectrum is always higher than the black one. It has undulations while the black spectrum is completely flat (as for the 80 Hz spectrum). The conclusion that can be drawn is that the high-frequency coherent signal is the source of the additional energy between the cyan and the black 20 Hz difference spectra, which is spread over the entire spectrum because of the aliasing.

4. Discussion of the results

The results presented in this study suggest that the SAR altimeter Sea Level Anomaly contains, depending on the sea state characteristics, some high-frequency coherent geophysical signal that is correlated to the presence of well-developed swells in the altimeter footprint. The argument supporting this statement is twofold. First, we observed that the peak wavenumber of the measured signal is close to the swell peak wavenumber. It is important to underline that it is true only if the signal is properly sampled, which is done by increasing the conventional posting rate from 20 Hz to 80 Hz. On this point, our study confirms the idea suggested by Reale et al. (2018) that sea-level undulations created by waves should always be aliased at 20 Hz sampling rate. Secondly, the time evolution of the signal, for which the use of Sentinel-3 tandem phase dataset was crucial, is consistent with waves traveling according to the linear deep-water wave dispersion relation. In other words, the phase shift measured on the cross-spectrum is well predicted by the phase velocity of the waves.

The observations are consistent with previous studies dealing with the effect of swell on SAR altimetry (Moreau et al., 2018; Raynal et al., 2018b), that reported an increase of the 1 Hz noise on the estimated parameters in the presence of swell. Indeed, the 1 Hz noise level (even if not directly analyzed here) integrates the variance of the high-frequency components of the signal and the spectral bump that was evidenced in this study contributes to it, in addition to the incoherent measurement noise. As the bump is due specifically to long swell waves, it makes sense that the measured 1 Hz noise level depends not only on the SWH, but also on the presence of long swell waves. Previous studies focused on the mean wave period T02 to characterize the effect of swell on SAR altimeter (Moreau et al., 2018; Raynal et al., 2018b), but the present results suggest it might be more relevant to consider the occurrence of a partition with long period, sufficiently high energy and favorable orientation. On the dependence of the 1 Hz noise to the wave period, our conclusion differs from the real data results obtained by Reale et al. (2018), who reported that the SAR mode 1 Hz noise depends only on the

SWH. However, as mentioned in the paper, their analysis focused on the North Sea, with relatively short period waves and hence the conclusions might not be applicable to the open ocean. Moreover, numerical simulations by Reale et al. (2020) seem to support the fact that the 1 Hz noise is impacted by the presence of long period waves.

The mechanisms through which waveforms (and, subsequently, the estimated parameters) are impacted by the presence of long waves in the altimeter footprint is out of the scope of this paper, and we think that it should be subject to a dedicated study. However, we believe that it is more complicated than a simple measurement of the wave topography on the altimeter track. To support this argument, we have plotted in Fig. 7 the S3A radargram for a small portion of the case D segment, as well as the corresponding uncorrected SLA, SWH and sigma naught parameters (for S3A and S3B). This plot shows that the observed SLA oscillations are not just created by a simple oscillation of the leading edge of the waveforms, but rather a consequence of the deformation of the whole waveform. We observe characteristic undulations on the trailing edge that were also reported in previous analyses (Moreau et al., 2018). Fig. 8 shows two consecutive S3A waveforms, extracted from the radargram of Fig. 7 around latitude -20.64° , which clearly exhibit such oscillations.

Moreover, as shown in Fig. 7, the SWH (and to a lesser extent the sigma naught) seems to be also impacted and exhibit similar high-frequency coherent signals. As suggested by (Moreau et al., 2018), the assumption of a Gaussian distribution of the scatterers height in the footprint might not be valid in the presence of swells whose wavelength is comparable to the footprint size in the along-track direction. In addition, other effects might also be implicated, such as the modulation of the backscattering by the slopes of the waves or the dynamical effects (azimuth smearing and velocity bunching) induced by the orbital velocities (Stopa et al., 2015; Buchhaupt, 2019). Finally, we also must keep in mind that the Delay-Doppler altimeter measurement process spans almost two seconds because of the incoherent stacking (multi-looking) that it implements (Raney, 1998). As the surface waves move during the measurement process, there should be some blurring in the data. Since all these effects are not properly modeled in the estimation of the parameters, the high-frequency SLA signal that is measured should be considered with care, maybe more as an error rather than accurate measurement of the wave topography.

The sea-state conditions for which the sea level signal is strong enough to emerge from the measurement noise have not been precisely characterized in the present paper. Relying on the individual cases, it seems that sea-states with well-developed swells (sharp peak in the very low frequency part of the wave spectrum), preferably oriented along the altimeter track, are favorable to the emergence of the oscillations in the estimated parameters. It is interesting to notice, as in case C for instance, that the swell does not have to be very strong, compared to the other components

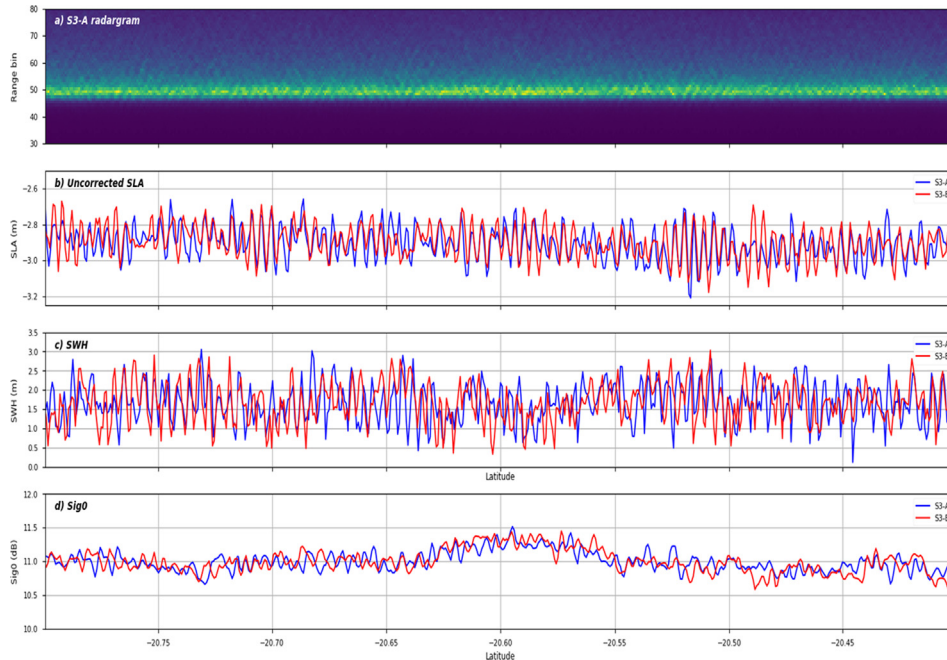


Fig. 7. Sentinel-3A waveforms (a) on a portion of the case D segment. Corresponding uncorrected SLA (b), SWH (c) and sigma naught (d) are plotted as a function of latitude.

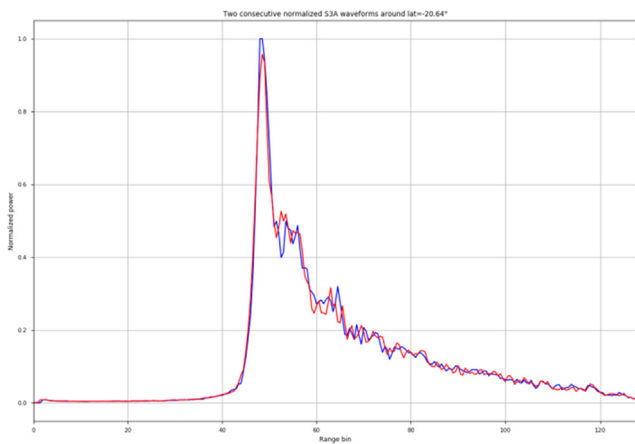


Fig. 8. Two consecutive 80 Hz S3A waveforms exhibiting oscillations on the trailing edge, induced by the swell.

of the wave spectrum. We also expect a cut-off effect due to the azimuth resolution, which prevents from being sensitive to wave periods smaller than 300 m (like in case A). These remarks suggest that the usual integrated sea-state parameters (SWH and wave mean periods) that have been used so far might not be the best parameters to characterize the sea-states prone to errors on the SAR-mode altimeter retrievals. Indicators of the presence of a long-wavelength swell component might be more appropriate in future studies.

As discussed before, the high-frequency signal evidenced in the present study can be viewed as an error resulting from abusive simplifications while modeling the sea-state in the waveform model. In our opinion, it is necessary to process the data with a high posting rate (80 Hz is used

in this study, but 40 Hz might be sufficient) to avoid the spectral aliasing that occurs at 20 Hz (which creates long-wavelength errors). Then, if there is the need to go back to lighter 20 Hz products, a low-pass filter should be applied before down sampling the data. Several filters could be envisaged, the simplest one being to apply a rolling average over four consecutive samples (for the 80 Hz case). This solution has been implemented and analyzed in (Egido et al., 2020), and it was shown that, in addition to the benefits that we expect in the present argumentation, it allows to reduce the level of the measurement noise. Fig. 9 shows the mean global SLA spectrum (using all

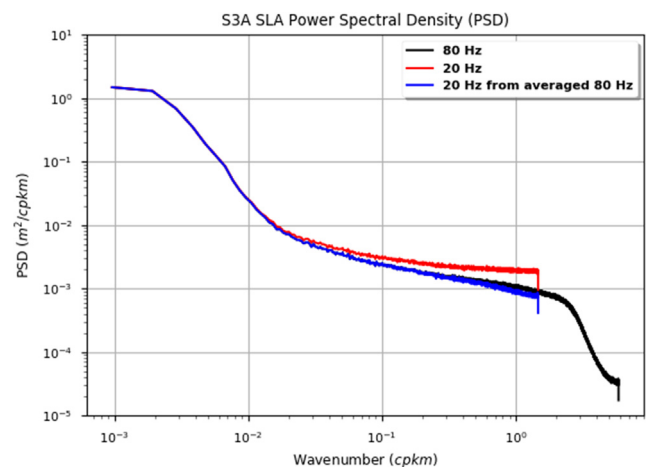


Fig. 9. Mean S3A SLA spectrum at 20 Hz (red), at 80 Hz (blue) and at 20 Hz after rolling average over four 80 Hz samples (black). (For interpretation of the references to color in this figure legend, the reader is referred to the web version of this article.)

the segments of the dataset) for raw 20 Hz (red), 80 Hz (black) and filtered 20 Hz (blue). We observe that the variance is reduced for the blue spectrum with respect to the red one, up to wavelength of 100 km.

Finally, we would like to stress the fact that this analysis has revealed one high-frequency effect related to swell, that could be easily identified among the incoherent noise thanks to the Sentinel-3 tandem phase dataset. However, sea states dominated by swell might also lead to long-wavelength biases that have not been addressed at all in this study. These potential effects are worth studying but the tandem phase would be of little interest to tackle these issues, as the mean parameters of the sea state are unchanged between the two acquisitions, leading to the same bias in both datasets.

5. Conclusion and perspectives

An important recommendation of this study is the use of azimuth oversampling for the unfocused SAR altimeter observations. Azimuth oversampling has already been proposed by [Egido et al., 2020](#), invoking the possible gain in measurement noise level, that was first reported by [Dinardo et al. \(2014\)](#). From our point of view, it allows to adequately sample high-frequency ocean wave signals under the Nyquist criterion, and thus mitigates aliasing artifacts. Under the latter condition, it might be possible to recover some valuable information about the sea state as the swell peak period, in a completely different and less heuristic approach than in [Gommenginger et al. \(2003\)](#). A more quantitative analysis is however required to assess the potential of these retrievals, and their benefit in enhancing altimeter products.

Similar analysis has been performed using the Fully Focused SAR (FF-SAR) processing ([Egido and Smith, 2017](#)) whose high-posting rate and high-resolution capabilities opened up an alternative way for studying the SSH signal induced by long wavelength waves ([Rieu et al., 2019](#)). The spectral signatures of the long waves were found to be comparable to those obtained from the 80-Hz unfocused SAR altimeter datasets. The FF-SAR technique did not provide much better insight into the SSH spectral content at higher frequencies because of the azimuth grating lobes (induced by the closed-burst pulsing of the Sentinel-3 altimeter) that alter FF-SAR data ([Egido & Smith, 2017](#); [Guccione et al., 2018](#)), acting as a band-stop filter on the spectrum. The Sentinel-6 radar altimeter, operating with open-burst pulsing (interleaved mode) ([Scharroo et al., 2016](#)) will probably enable to fully benefit from the FF-SAR processing capabilities and provide much more details of the ocean surface structures, possibly down to few tens of meters (as long as the signal to noise ratio is sufficiently low).

As an alternative processing strategy, it has been demonstrated that by averaging the beams from the same fan, thus enlarging the effective footprint to the conventional altimetry one, allows to mitigate the impact of the

long ocean waves on the SAR-mode altimeter retrievals. This approach is the one used in the LR-RMC processing method ([Boy et al., 2017b](#)) whose low sensitivity to swells had already been proven to be effective and its high performance to better observe ocean mesoscale structures demonstrated.

Results that emerge from this study yield novel insights into our understanding of the impact of swell on SAR altimetry. Additional analyses are now required to answer further questions such as the occurrences of these effects (locally and globally), and whether long ocean wave effects cause spurious trends in the altimeter climate record. In view of that, this paper puts forward new SAR altimeter processing approaches to optimally mitigate these effects. This concern is shared by the Copernicus Marine Environment Monitoring Service which primary objective is currently to provide the highest possible Sentinel-3 data quality to users. It is also of high importance for the upcoming missions that tend toward more use of SAR altimeter in the future. Besides that, this study underlines the usefulness of a two-satellite close formation constellation for detecting rapidly evolving phenomenon, like propagating swells, in a more efficient way than with a single satellite mission. Future altimeter tandem phases should consider the benefit to be gained in acquiring datasets with different time intervals. The same kind of analyses could be applied for studying other ocean processes impacting altimetry measurements that have larger time and spatial scales, like internal solitary waves (ISW) ([Santos-Ferreira et al., 2018](#)) or sigma naught bloom events ([Mitchum et al., 2004](#)).

Declaration of Competing Interest

The authors declare that they have no known competing financial interests or personal relationships that could have appeared to influence the work reported in this paper.

Acknowledgment

The authors acknowledge the usefulness of having the L1A SRAL PDGS products available for conducting advanced SAR altimeter investigations like the present study.

This research was supported by the Sentinel-3 Tandem for Climate (S3TC) ESA project.

The authors would like to thank Salvatore Dinardo and Gérald Dibarboure for valuable discussions and IFREMER for the provision of the WW3 products.

References

- Abdalla, S., S. Dinardo, “Does swell impact SWH from SAR altimetry?”, 2016 SAR Altimetry Workshop, La Rochelle, France, Oct. 31, 2016 (Available online at https://meetings.aviso.altimetry.fr/fileadmin/user_upload/tx_ausycslseminar/files/OSTST2016/SAR_03_Abdalla_SAR_WS_20161031.pdf)

- Aldarias, A., J. Gómez-Enri, I. Laiz, B. Tejedor, S. Vignudelli and P. Cipollini (2020), “Validation of Sentinel-3A SRAL Coastal Sea Level Data at High Posting Rate: 80 Hz,” *IEEE Trans. Geosci. Remote Sens.*, doi: 10.1109/TGRS.2019.2957649.
- Ardhuin, F., Stopa, J.-E., Chapron, B., Collard, F., Husson, R., Jensen, R.-E., Johannessen, J., Mouche, A., Passaro, M., Quartly, G.-D., Swail, V., Young, I., 2019. Observing Sea States. *Front. Mar. Sci.* 6, 124. <https://doi.org/10.3389/fmars.2019.00124>.
- Aouf, L. and Phalippou, L., “On the signature of swell for the Cryosat-2 SAR-mode wave data”, OSTST Meeting 2015, Reston, Virginia, USA, Oct. 20 – Oct. 23, 2015 [Available online at https://meetings.avisio.altimetry.fr/fileadmin/user_upload/tx_ausycslsseminar/files/OSTST2015/IPM-02-ostst_Aouf_sarmode_2015_1.pdf].
- Boisot, O., Amarouche, L., Lalaurie, J.-C., Guérin, C.-A., 2016. Dynamical Properties of Sea Surface Microwave Backscatter at Low-Incidence: Correlation Time and Doppler Shift. *IEEE Trans. Geosci. Remote Sens.* 54, 7385–7395. <https://doi.org/10.1109/TGRS.2016.2601242>.
- Boy, F., Desjonquères, J.-D., Picot, N., Moreau, T., Raynal, M., 2017a. CRYOSAT-2 SAR Mode Over Oceans: Processing Methods, Global Assessment and Benefits. *IEEE Trans. Geosci. Remote Sens.* 55, 148–158. <https://doi.org/10.1109/TGRS.2016.2601958>.
- Boy, F., T. Moreau, P. Thibaut, P. Rieu, J. Aublanc, N. Picot, P. Féménias, C. Mavrocordatos (2017b), New stacking method for removing the SAR sensitivity to swell, OSTST Meeting 2017, Miami, Florida, USA, Oct. 23-27, 2017
- Buchhaupt, C., Fenoglio, L., Becker, M., 2018. SAR-RDSAR: A new Service on G-POD for SAR and RDSAR Products. *EGU General Assembly Conference Abstracts* 20, 16789.
- Buchhaupt, C. (2019), Model Improvement for SAR Altimetry. Darmstadt, Schriftenreihe Fachrichtung Geodäsie der Technischen Universität Darmstadt, Technische Universität, ISBN 978-3-935631-44-0, [Ph.D. Thesis], <https://tuprints.ulb.tu-darmstadt.de/9015>.
- Carter, G., Knapp, C., Nuttall, A., 1973. Estimation of the magnitude-squared coherence function via overlapped fast Fourier transform processing. *IEEE Trans. Audio Electroacoustics* 21 (4), 337–344. <https://doi.org/10.1109/TAU.1973.1162496>.
- Chelton, D. B., Ries, J. C., Haines, B. J., Fu, L.-L., & Callahan, P. S. (2001), “Chapter 1: Satellite Altimetry. Satellite Altimetry and Earth Sciences - A Handbook of Techniques and Applications,” *International Geophysics*, 69, 1–131, doi: 10.1016/s0074-6142(01)80146-7.
- Chen, G., Chapron, B., Ezraty, R., Vandemark, D., 2002. A global view of swell and wind sea climate in the ocean by satellite altimeter and scatterometer. *J. Atmos. Oceanic Technol.* 19, 1849–1859. [https://doi.org/10.1175/1520-0426\(2002\)019<1849:AGVOSA>2.0.CO;2](https://doi.org/10.1175/1520-0426(2002)019<1849:AGVOSA>2.0.CO;2).
- Clerc, S., Donlon, C., Borde, F., Lamquin, N., Hunt, S.E., Smith, D., McMillan, M., Mittaz, J., Woolliams, E., Hammond, M., Banks, C., Moreau, T., Picard, B., Raynal, M., Rieu, P., Guérin, A., 2020. Benefits and lessons learned from the Sentinel-3 Tandem phase. *Remote Sens.* 12 (17), 2668. <https://doi.org/10.3390/rs12172668>.
- Dibarboure, G., Pujol, M.-I., Briol, F., Le Traon, P.-Y., Larnicol, G., Picot, N., Mertz, F., Ablain, M., 2011. Jason-2 in DUACS: First tandem results and impact on processing and products. *Mar. Geod.* 34 (3–4), 214–241. <https://doi.org/10.1080/01490419.2011.584826>.
- Dibarboure, G., Boy, F., Desjonquères, J.D., Labroue, S., Lasne, Y., Picot, N., Thibaut, P., 2014. Investigating short-wavelength correlated errors on low-resolution mode altimetry. *J. Atmos. Oceanic Technol.* 31 (6), 1337–1362. <https://doi.org/10.1175/JTECH-D-13-00081.1>.
- Dinardo, S., B. Lucas and J. Benveniste, “SAR altimetry at 80 Hz”, OSTST Meeting 2014, Lake Constance, Germany, Oct. 28 – Oct. 31, 2014 [Available online at https://meetings.avisio.altimetry.fr/fileadmin/user_upload/tx_ausycslsseminar/files/SAR_Altimetry_at_80_Hz_OSTST_2014.pdf]
- Dinardo, S., Restano, M., Ambrósio, A., & Benveniste, J. (2016), “SAR altimetry processing on demand service for Cryosat-2 and Sentinel-3 AT ESA G-POD,” In *Proceedings of the 2016 conference on Big Data from Space (BiDS’16)*, Santa Cruz de Tenerife, Spain, pp. 15-17.
- Donlon, C., Berruti, B., Buongiorno, A., Ferreira, M.-H., Féménias, P., Frericka, J., Goryl, P., Kleina, U., Laur, H., Mavrocordatos, C., et al., 2012. The Global Monitoring for Environment and Security (GMES) Sentinel-3 mission. *Rem. Sens. Environ.* 120, 37–57. <https://doi.org/10.1016/j.rse.2011.07.024>.
- Egido, A., Smith, W.H.F., 2017. Fully focused SAR altimetry: theory and applications. *IEEE Trans. on Geosci. Remote Sens.* 55 (1), 392–406. <https://doi.org/10.1109/TGRS.2016.2607122>.
- Egido, A., S. Dinardo, and C. Ray (2020), “The case for increasing the posting rate in delay/Doppler altimeters”, *Adv. Space Res.*, doi: 10.1016/j.asr.2020.03.014.
- Gommenginger, C.P., Srokosz, M.A., Challenor, P.G., Cotton, P.D., 2003. Measuring ocean wave period with satellite altimeters: A simple empirical model. *Geophys. Res. Lett.* 30 (22). <https://doi.org/10.1029/2003gl017743>.
- Guccione, P., Scagliola, M., Giudici, D., 2018. 2D Frequency Domain Fully Focused SAR Processing for High PRF Radar Altimeters. *Remote Sens.* 10 (12), 1943. <https://doi.org/10.3390/rs10121943>.
- Halimi, A., Mailhes, C., Tourneret, J.-Y., Thibaut, P., Boy, F., 2014. A semi-analytical model for delay/Doppler altimetry and its estimation algorithm. *IEEE Trans. Geosci. Remote Sens.* 52 (7), 4248–4258. <https://doi.org/10.1109/tgrs.2013.2280595>.
- Holthuijsen, L.H., 2010. *Waves in oceanic and coastal waters*. Cambridge University Press, pp. 4–5.
- Le Gac, S., Boy, F., Blumstein, D., Lasson, L., Picot, N., 2019. Benefits of the Open-Loop Tracking Command (OLTC): Extending conventional nadir altimetry to inland waters monitoring. *Adv. Space Res.* <https://doi.org/10.1016/j.asr.2019.10.031>.
- Mitchum, G.T., Hancock III, D.W., Hayne, G.S., Vandemark, D.C., 2004. Blooms of σ_0 in the TOPEX Radar Altimeter Data. *J. Atmospheric Oceanic Technol.* 21 (8), 1232–1245. [https://doi.org/10.1175/1520-0426\(2004\)021<1232:BOITTR>2.0.CO;2](https://doi.org/10.1175/1520-0426(2004)021<1232:BOITTR>2.0.CO;2).
- Moreau, T., Tran, N., Aublanc, J., Tison, C., Le Gac, S., Boy, F., 2018. Impact of long ocean waves on wave height retrieval from SAR altimetry data. *Adv. Space Res.* 62 (6), 1434–1444. <https://doi.org/10.1016/j.asr.2018.06.004>.
- Pires N., Fernandes M. J., Gommenginger C. and Scharroo R., 2016,” A conceptually simple modeling approach for Jason-1 sea state bias correction based on 3 parameters exclusively derived from altimetric information,” *Remote Sens.*, 8(7), 576. doi: 10.3390/rs8070576.
- Portilla, J., Ocampo-Torres, F.J., Monbaliu, J., 2009. Spectral partitioning and identification of wind sea and swell. *J. Atmos. Oceanic Technol.* 26 (1), 107–122. <https://doi.org/10.1175/2008JTECHO609.1>.
- Raney, R.K., 1998. The delay/doppler radar altimeter. *IEEE Trans. Geosci. Remote Sens.* 36 (5), 1578–1588. <https://doi.org/10.1109/36.718861>.
- Rasclé, N., Ardhuin, F., 2013. A global wave parameter database for geophysical applications. Part 2: model validation with improved source term parameterization. *Ocean Modell.* 70, 174–188. <https://doi.org/10.1016/j.ocemod.2012.12.001>.
- Ray, C., Martin-Puig, C., Clarizia, M.P., Ruffini, G., Dinardo, S., Gommenginger, C., et al., 2015. “SAR altimeter backscattered waveform model,” *IEEE Trans. Geosci. Remote Sens.* 53, 911–919. <https://doi.org/10.1109/TGRS.2014.2330423>.
- Raynal, M., Labroue, S., Moreau, T., Boy, F., Picot, N., 2018a. From Conventional to Delay Doppler Altimetry: a Demonstration of Continuity and Improvements with Cryosat-2 mission. *Adv. Space Res.* 62 (6), 1564–1575. <https://doi.org/10.1016/j.asr.2018.01.006>.
- Raynal, M., T. Moreau, N. Tran, S. Labroue, F. Boy, P. Féménias and F. Borde, “Assessment of the SARM processing sensitivity to swell”, OSTST Meeting 2018, Ponta Delgada, Portugal, Sept. 27 - Sept. 28, 2018b. Available online at https://meetings.avisio.altimetry.fr/fileadmin/user_upload/ERR_01_Raynal.pdf.
- Reale, F., Dentale, F., Carratelli, E.P., Fenoglio-Marc, L., 2018. Influence of Sea State on Sea Surface Height Oscillation from Doppler Altimeter Measurements in the North Sea. *Remote Sens.* 10 (7), 1100. <https://doi.org/10.3390/rs10071100>.

- Reale, F., Pugliese Carratelli, E., Di Leo, A., Dentale, F., 2020. Wave orbital velocity effects on radar Doppler altimeter for sea monitoring. *J. Marine Sci. Eng.* 8 (6), 447. <https://doi.org/10.3390/jmse8060447>.
- Rieu, P., T. Moreau, M. Raynal, P. Thibaut, C. Donlon, F. Borde, F. Boy, N. Picot and S. Clerc, “First SAR altimeter tandem phase: a unique opportunity to better characterize open ocean SAR altimetry signals with unfocused and focused processing”, OSTST Meeting 2019, Chicago, IL, USA, Oct. 21 – Oct. 25, 2019 [Available online at] https://meetings.avisio.altimetry.fr/fileadmin/user_upload/2019/IPM_08_RieuOSTST_2019_FFSAR_ocean_v1.pdf.
- Santos-Ferreira, A.M., Da Silva, J.C., Magalhaes, J.M., 2018. SAR Mode Altimetry Observations of Internal Solitary Waves in the Tropical Ocean Part 1: Case Studies. *Remote Sens.* 10 (4), 644. <https://doi.org/10.3390/rs10040644>.
- Scagliola, M. (2013), “CryoSat Footprints,” Aresys Technical Note, 1.1., Technical Report SAR-CRY2-TEN-6331, ESA. [Available online at] https://earth.esa.int/documents/10174/125271/CryoSat_Footprints_TN_v1.1.1.pdf.
- Scharroo, R., Bonekamp, H., Ponsard, C., Parisot, F., von Engeln, A., Tahtadjev, M., de Vriendt, K., Montagner, F., 2016. Jason continuity of services: continuing the Jason altimeter data records as Copernicus Sentinel-6. *Ocean Sci.* 12, 471–479. <https://doi.org/10.5194/os-12-471-2016>.
- Stopa, J.E., Arduin, F., Chapron, B., Collard, F., 2015. Estimating wave orbital velocity through the azimuth cutoff from space-borne satellites. *J. Geophys. Res: Oceans* 120 (11), 7616–7634. <https://doi.org/10.1002/2015jc011275>.
- Tran, N., D. Vandemark, S. Labroue, H. Feng, B. Chapron, H. L. Tolman, J. Lambin and N. Picot (2010), “Sea state bias in altimeter sea level estimates determined by combining wave model and satellite data,” *J. Geophys. Res.*, 115, C03020, doi: 10.1029/2009JC005534.
- Tran, N., Vandemark, D., Zaron, E.D., Thibaut, P., Dibarboue, G. and Picot, N. (2020), “Assessing the effects of sea-state related errors on the precision of high-rate Jason-3 altimeter sea level data,” *Adv. Space Res.*, doi: 10.1016/j.asr.2019.11.034.
- Vergara, O., Morrow, R., Pujol, I., Dibarboue, G., Ubelmann, C., 2019. Revised global wavenumber spectra from recent altimeter observations. *J. Geophys. Res.* 124 (6), 3523–3537. <https://doi.org/10.1029/2018JC014844>.
- Welch, P., 1967. The use of fast Fourier transform for the estimation of power spectra: a method based on time averaging over short, modified periodograms. *IEEE Trans. Audio Electroacoust.* 15 (2), 70–73. <https://doi.org/10.1109/TAU.1967.1161901>.
- Wingham, D.J., Francis, C.R., Baker, S., Bouzinac, C., Brockley, D., Cullen, R., de Chateau-Thierry, P., Laxon, S., Mallow, U., Mavrocordatos, C., Phalippou, L., Ratier, G., Rey, L., Rostan, F., Viau, P., Wallis, D., 2006. CryoSat: a mission to determine the fluctuations in Earth’s land and marine ice fields. *Adv. Space Res.* 37 (4), 841–871. <https://doi.org/10.1016/j.asr.2005.07.027>.
- Zaron, E.D., deCarvalho, R., 2016. Identification and Reduction of Retracker-Related Noise in Altimeter-Derived Sea Surface Height Measurements. *J. Atmos. Oceanic Technol.* 33 (1), 201–210. <https://doi.org/10.1175/jtech-d-15-0164.1>.